communications materials

Article

https://doi.org/10.1038/s43246-024-00473-9

Locally controlled MOF growth on functionalized carbon nanotubes

Marvin J. Dzinnik[1] ✉, Necmettin E. Akmaz[1], Adrian Hannebauer[2], Andreas Schaate[2], Peter Behrens[2,3,4] & Rolf J. Haug[1,3]

Metal-organic frameworks (MOFs) are highly versatile materials because of their tunable properties. However, the typically poor electrical conductivity of MOFs presents challenges for their integration into electrical devices. By adding carbon nanotubes to MOF synthesis, a highly intergrown material with increased conductivity and chemiresistive sensing properties can be obtained. Here, we present a patterning technique to control MOF growth on predefined areas of one particular carbon nanotube. We found that electron beam pretreatment of -COOH functionalized multi-walled carbon nanotubes inhibits the growth of UiO-66 MOF on these multi-walled carbon nanotubes. By irradiating individual multi-walled carbon nanotubes, we show that MOF growth can be inhibited in predefined tube areas, creating MOF-free spaces on the nanotube. In this way, our method shows a possibility to pattern MOF growth on individual nanotubes.

Metal-organic frameworks (MOFs) are porous materials built from metallic ion clusters and organic linker molecules[1]. Important properties, such as pore size, electrical conductance, or chemical activity, are strongly dependent on the combination of these building blocks[2]. The properties can be further adjusted by modification of linker molecules or metallic clusters or by incorporating atoms, nanoparticles, or nanostructures into the MOF[3,4]. These changes can be made in situ[5] or post-synthetic[6]. This freedom in tunability makes them applicable in many fields, for instance, for helium[7] or hydrogen[8] separation, for catalysis[9] and as gas sensors[10–12] like for methanol[13] sensing.

Conductive MOFs are essential for chemiresistive sensing applications[14]. There are several design strategies to promote the conductance of MOF materials, among others, to tune the charge transport over an extended conjugation pathway, a through-bond pathway, or a through-space pathway[15–17]. Other mechanism to promote charge transport in MOFs without changing the building blocks of a specific MOF is to load the pores with redox-active guest molecules[18] or by adding conductive materials[12,19,20]. Carbon nanotubes (CNTs) have emerged as prominent additives due to their high surface area and high current carrying capacity[21–24]. The functionalization of CNTs plays a key role in the in situ synthesis of MOF/CNT composites[23]. MOF synthesis in the presence of functionalized CNTs enables direct MOF growth on the surface of the tubes[25–27]. In particular, UiO-66[28] grows preferentially on carboxyl (-COOH) functionalized carbon nanotubes[5,29,30]. An explanation for this is the chemical similarity between the UiO-66 linker molecules and the -COOH functionalization of the tubes. UiO-66 is one of the best-suited MOFs for sensing applications due to its remarkable thermal and chemical stability, especially its high stability against moisture. Networks of many multi-walled carbon nanotubes (MWCNTs) with UiO-66 MOF were shown to exhibit chemiresistive ethanol sensing properties that are absent in bare CNTs[5]. MOF/CNT hybrid structures with other MOFs have shown detection capabilities for substances such as lead[31], H_2O_2[25], nitride[26], humidity[27], and others[19,23].

Originally, CNT surface functionalization was introduced as a standard procedure to enhance the dispersibility of CNTs in solvents[32]. Typically, this involves oxidation to introduce carboxyl and hydroxyl groups to the tube surface[24], while also removing catalytic metal residues and amorphous carbon[32]. It should be noted that this process is reversible; defunctionalization of functionalized carbon nanotubes in a solvent leads to the formation of large clusters of entangled tubes[33].

Here in this work, electron beam-controlled, UiO-66 MOF patterning on functionalized MWCNTs is presented. Precise local control of MOF growth is crucial for complex device architectures, such as e.g., necessary for miniaturized nanosensor arrays. In previous studies, MOF patterning[34] was performed using different methods[35–39], e.g., by decorating substrates with surface-modified nanoparticles and utilizing the aligned particles as nucleation sites[40–42]. In contrast to these methods, our method involves inhibition of MOF growth by spatial deactivation of nucleation sites. The mechanism is shown schematically in Fig. 1. First, we deposited -COOH

[1]Institut für Festkörperphysik, Leibniz Universität Hannover, Hannover, Germany. [2]Institut für Anorganische Chemie, Leibniz Universität Hannover, Hannover, Germany. [3]Laboratorium für Nano- und Quantenengineering, Leibniz Universität Hannover, Hannover, Germany. [4]Deceased.
✉e-mail: dzinnik@nano.uni-hannover.de

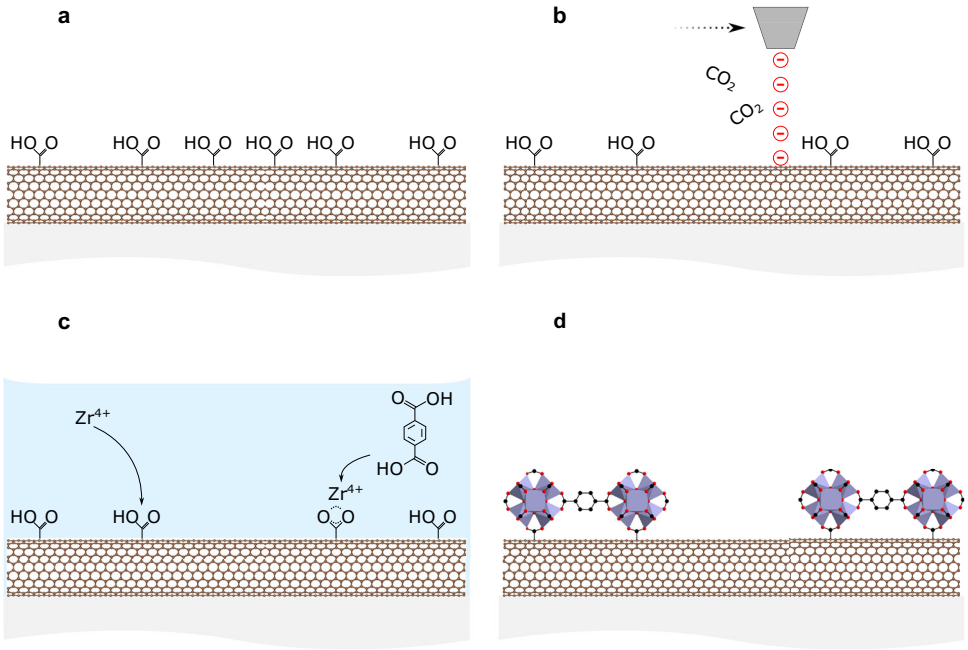

Fig. 1 | Schematic illustration of the UiO-66 growth inhibition mechanism. a COOH functionalized multi-walled carbon nanotube (MWCNT). The functionalization molecules are shown only on the top site and not around the tube for the sake of clarity (not to scale). **b** Irradiation and local defunctionalization by an electron beam. **c** Locally irradiated MWCNT in an UiO-66 synthesis solution, which contains Zr-salt, linker molecules, and additives. The Zr^{4+}-ions bind to the functionalization, seeding the growth of the MOF. **d** After synthesis. UiO-66 crystals have grown on the MWCNT. Growth is inhibited in the irradiated areas.

functionalized MWCNTs on a Si chip with SiO_2 surface by drop-casting (Fig. 1a). The individual MWCNTs are then locally irradiated by an electron beam, resulting in defunctionalization of the MWCNTs (Fig. 1b). Subsequently, the chip is placed in an UiO-66 synthesis solution containing Zr-salt, linker molecules, and additives (Fig. 1c; synthesis details are provided in the Methods section). Growth can occur in tube areas that were not irradiated. This can be explained by an intact functionalization of the MWCNT that possibly acts as a coordination center for the Zr^{4+}-ions allowing MOF nucleation on the surface of the MWCNT (Fig. 1d)[5,29,30]. Scanning electron microscope (SEM) imaging was used to quantify the MOF growth. Our method allows to pattern the growth of MOF crystals locally on individual MWCNTs.

Results and discussion

Electron beam-induced growth inhibition

Figure 2 shows the influence of electron irradiation on the growth of UiO-66 crystals (crystallinity verified with powder X-ray diffraction, PXRD, data shown in Supplementary Note 1) on various MWCNTs. Initially, MWCNTs were found to be around 35 nm thick and individual tubes are clearly distinguishable, as shown in Fig. 2a. After synthesis and without prior irradiation, thick MOF crystals fully encapsulate the MWCNTs, leaving no visible tube area, as shown in Fig. 2b. The -COOH functionalization acts as a seed for UiO-66 MOF growth and the MOF crystals grow preferred on such functionalized MWCNTs[5]. In contrast to this, Fig. 2c shows an image of an area irradiated with a dose $D = 9000$ μC cm^{-2} at an acceleration voltage $V_{acc} = 6$ kV. The irradiation prior to synthesis leads to strongly inhibited MOF growth. Only very few MOF crystals have grown on the MWCNTs. Interestingly, the combination of higher electron energies, due to a higher acceleration voltage, and a higher dose results in a less distinct growth inhibition. This can be seen in Fig. 2d. The area was irradiated by electrons accelerated at $V_{acc} = 30$ kV and a dose $D = 10{,}000$ μC cm^{-2}. Notably, oxidized graphene, which has a similar structure to our functionalized MWCNTs, exibits an electron beam-induced defunctionalization effect at an acceleration voltage of $V_{acc} = 80$ kV[43]. In the case of MWCNTs in solution, UVC irradiation has been found to induce a process known as photodecarboxylation, resulting in the defunctionalization of MWCNTs functionalized with -COOH molecules[33]. Drawing parallels from these findings, our observation of MOF growth inhibition on MWCNTs by electron irradiation, as seen in Fig. 2c and d, can be attributed to a similar defunctionalization effect. A -COOH defunctionalization is also supported by X-ray photoelectron spectroscopy (XPS) analysis of MWCNTs before and after electron irradiation (XPS data shown in Supplementary Note 1).

Impact of the electron dose

To study the dose-dependent growth inhibition in more detail, we systematically irradiated areas with various MWCNTs by different doses, prior to UiO-66 synthesis. Figure 3 shows SEM images of MWCNTs after synthesis, with MWCNTs colored in red and MOF crystals colored in blue (for the uncolored images, see Supplementary Note 2). The areas presented were irradiated with increasing doses at a fixed electron acceleration voltage $V_{acc} = 6$ kV. For the lowest dose $D = 1000$ μC cm^{-2} (Fig. 3a) minor changes in MOF growth are observed, compared to the non-irradiated case (see Fig. 2b). Most of the MWCNTs are covered by MOF (blue area), and only small parts of the bare MWCNTs (red area) are visible. However, in contrast to the non-irradiated case, individual MOF grains become distinguishable. An irradiation dose of $D = 2000$ μC cm^{-2} further inhibits the growth of MOF (Fig. 3b) and the crystal size of the MOF appears to be reduced. MOF crystals are separated from each other, and the MWCNTs can be recognized. The areas irradiated by a further increased dose $D = 3000$ μC cm^{-2} (Fig. 3c) follow this trend. Fewer MOF crystals grow on the MWCNTs and large parts of the MWCNTs are visible. MWCNTs in areas irradiated by $D = 5000$ μC cm^{-2} (Fig. 3d) show strongly inhibited MOF growth and only a small number of MOF crystals have grown on the MWCNTs.

Impact of the electron acceleration voltage

We also analyzed the dose dependence on growth inhibition for irradiation with higher energy electrons using an acceleration voltage of $V_{acc} = 30$ kV. To quantify the different impacts of $V_{acc} = 6$ kV and $V_{acc} = 30$ kV, the MOF covered area A_{MOF} was determined directly from SEM images (see Supplementary Note 2). Similarly, the visible areas of the MWCNTs were determined. From the highest dose values $D \geq 6000$ μC cm^{-2} (strong growth inhibition), the mean area of MWCNTs $A_{CNTmean}$ in the images was approximated. The ratio $A_{MOF}/A_{CNTmean}$ for different irradiation doses D at $V_{acc} = 6$ kV is shown in Fig. 4a. The decrease in MOF area is well described

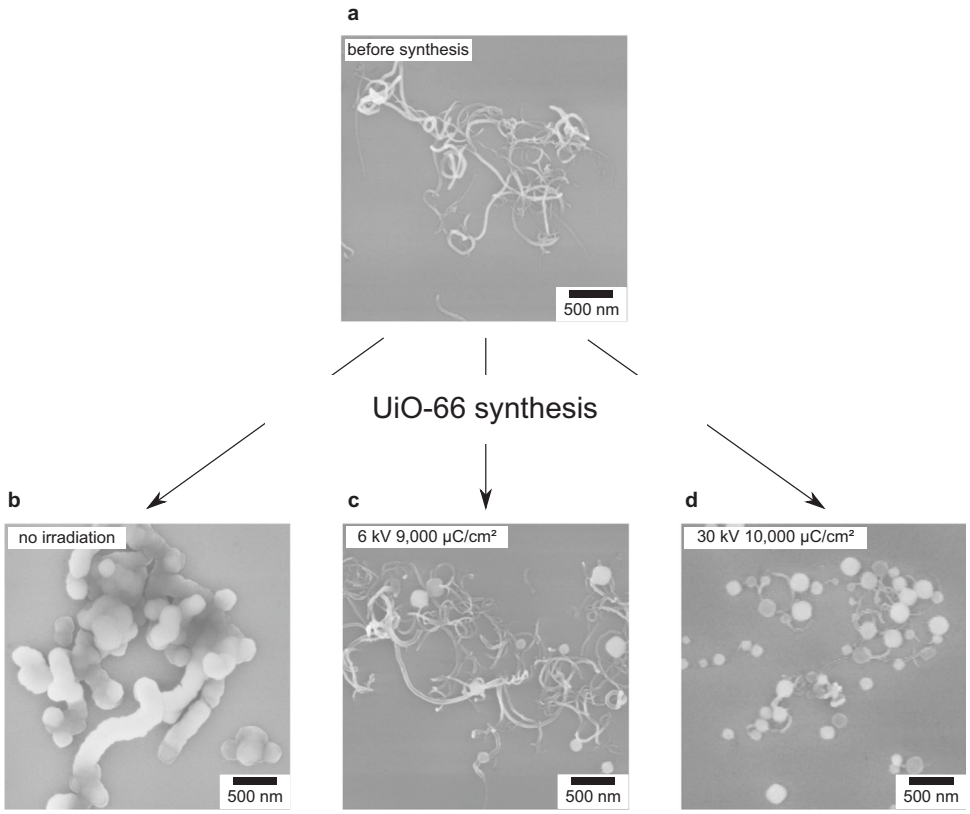

Fig. 2 | MOF growth inhibition by electron irradiation. a Typical scanning electron microscope image of multi-walled carbon nanotubes (MWCNTs) *before* MOF synthesis. **b**, **c**, and **d** are images *after* UiO-66 MOF synthesis. **b** Non-irradiated MWCNTs, **c** V_{acc} = 6 kV and D = 9000 µC cm^{-2} and **d** V_{acc} = 30 kV and D = 10,000 µC cm^{-2}.

by an exponential decrease of the form $A_{MOF}/A_{CNTmean} = A \cdot \exp(-D/g)$ with $A_{6kV} = 4$ and $g_{6kV} = 1785$ µC cm^{-2}. This is also the case when using electrons of higher energy accelerated by V_{acc} = 30 kV, as seen in Fig. 4b. The exponential fit is described with the parameters $A_{30kV} = 4.5$ and $g_{30kV} = 5271$ µC cm^{-2}. At this increased acceleration voltage, the growth inhibiting effect is less pronounced in contrast to V_{acc} = 6 kV. In both cases (V_{acc} = 6 kV and V_{acc} = 30 kV) the used acceleration voltages generate electrons with kinetic energies that are several orders of magnitude higher than typical organic binding energies (range of eV). The acceleration voltage has strong impacts on the electron penetration depth in the substrate and the backscattering (Electron scattering simulations can be found in Supplementary Note 2). Figure 4c illustrates the backscattering effect (e.g., V_{acc} = 6 kV). Electrons from an incoming electron beam (red) penetrate the surface, are absorbed in the substrate, and they lose energy. Secondary electrons are backscattered and return to the surface[44] (blue). These electrons contribute to the defunctionalization process. Figure 4d illustrates the scattering for a higher acceleration voltage (e.g., V_{acc} = 30 kV) than in Fig. 4c. Electrons penetrate deeper into the substrate before scattering, and fewer electrons reach the surface. In this case, there are fewer electrons that contribute to the defunctionalization process.

Locally controlled MOF growth

This knowledge was now used to locally deplete the growth of MOF crystals in specific areas of individual MWCNTs. Before MOF synthesis, stripes of s = 200 nm width crossing the MWCNTs were irradiated at an acceleration voltage V_{acc} = 6 kV. Irradiation with different doses results in MOF-free areas with certain lengths that are different from the stripe width s = 200 nm. Colored SEM images of these MWCNTs can be seen in Fig. 5a–c (MOF colored in blue, bare MWCNT colored in red). Figure 5a shows a MWCNT irradiated by D = 8000 µC cm^{-2}, resulting in a MOF-free area of 470 nm length along the tube, this is larger than the initial stripe width s = 200 nm. Lowering the irradiation dose reduces the lengths of the MOF-free tube area, as seen in Fig. 5b (see Supplementary Note 3). We were able to achieve a MOF-free tube area of 220 nm length along the tube by using D = 6000 µC cm^{-2}. By using D = 4000 µC cm^{-2}, as shown in Fig. 5c, a MOF-free tube area of 130 nm length was obtained although the width of the irradiated stripe was s = 200 nm. Defunctionalization by electron scattering is a statistical process, and lowering the dose leads to a higher probability of remaining functional molecules, resulting in a possibly shorter length of the MOF-free tube area compared to that initially irradiated. The observed enlargement of the MOF-free area along the length of the tube, as shown in Fig. 5a, b, can be explained by defunctionalization outside the irradiated tube length s, due to randomly off-axis backscattered electrons, as shown schematically in Fig. 5d.

Our technique shows how to nanopattern the growth of MOF crystals on the scale of an individual MWCNT. This allows to restrict MOF growth to specific tube areas. Possible applications would be more complex devices, such as MOF/CNT transistors with MOF dielectrics or MOF/CNT nanosensor arrays.

Because this process is explained by the removal of functional molecules on the MWCNT, other defunctionalization methods, such as EUV or UVC irradiation, should show similar results. The described working principle also indicates the possibility of expanding this process to other MOF species, as well as to other functionalized materials.

Conclusion

In conclusion, the impact of electron irradiation on the growth of UiO-66 MOF on functionalized MWCNTs was studied. In non-irradiated areas, MWCNTs were found to be fully encapsulated by the MOF. However, in irradiated areas, the growth of MOF crystals was inhibited, with stronger inhibition at higher irradiation doses. We attribute this to the defunctionalization of the MWCNTs by backscattered electrons. Lower acceleration voltages result in stronger growth inhibition than higher ones. Electrons accelerated by lower voltages penetrate the substrate less deeply and more electrons are backscattered to the surface. With this process, we are able to locally deplete the growth of MOF crystals on individual MWCNTs. This process opens the way to nanofabricate complex MOF/MWCNT

devices based on a single nanotube as e.g., needed in applications as nanosensors.

Methods

Chemicals

Zirconium (IV) chloride (>99.5%, $ZrCl_4$, Sigma Aldrich), N,N-dimethylformamide (99.8%, DMF, Sigma Aldrich), formic acid (>98%, HCOOH, Merck), terephthalic acid (99%, $C_8H_6O_4$ (H_2BDC), Honeywell), denatured ethanol (96%, C_2H_5OH, Sigma Aldrich), nitric acid (70%, HNO_3, Sigma Aldrich), acetone (99.8%, C_3H_6O, Carl Roth), isopropanol (99.8%, 2-propanol, C_3H_8O, Carl Roth) were used without purification.

Carbon nanotube preparation

Multi-walled carbon nanotubes (Baytubes C 70 P, Bayer) with diameters around 35 nm and length of several microns were oxidized for 6 hours in boiling nitric acid. This step adds a carboxy functionalization to the surface of the tube. An ethanol solution with 0.001 m% oxidized MWCNTs was prepared. Around 10–20 µL of the MWCNT/ethanol solution was deposited by drop-casting on a 4×4 mm^2 chip. Standard N++/As doped <100> silicon wafer with 340 nm thermally grown silicon dioxide, provided by Si-Mat, were used as chip material. Arrays of gold/chrome markers served for orientation (the gold/chrome markers are shown in Supplementary Note 2). Before drop-casting, the chips were ultrasonically cleaned (Elma Elmasonic S 30 H) for 10 min in acetone, washed in isopropanol, then cleaned by oxygen plasma for 5 min and 200 W (TePla Plasma Prozessor 100-E) and subsequently ultrasonically cleaned in acetone for 5 min and washed again in isopropanol.

Electron beam lithography

A scanning electron microscope (SEM) LEO 1530 with a Raith Elphy Nanolithography system was used to irradiate squares of 5000 µm^2 with doses up to 10,000 µC cm^{-2} and lines of 200 nm width and doses up to 10,500 µC cm^{-2} at acceleration voltages of either 6 kV or 30 kV. The squares were at least 100 µm and the stripes 4.8 µm apart from each other.

The same system was used for SEM imaging.

Synthesis of UiO-66/MWCNT composite

The UiO-66/MWCNT composites were synthesized according to a synthesis method developed in the Behrens group[5]. UiO-66/MWCNT was synthesized in a 100 mL Pyrex glass vessel by sequentially adding 0.1003 g $ZrCl_4$ (1 Eq), 0.031 mL deionized water (4 Eq), 0.812 mL formic acid (50 Eq) and 0.0715 g H_2BDC (1 Eq) in 25 mL DMF (750 Eq). The synthesis solution was ultrasonicated for 5 min to ensure that the Zr-salt and the linker were completely dissolved. The SiO_2/Si chip with MWCNTs on it was carefully added to the solution and placed top-up at the bottom of the glass vessel. The glass vessel was sealed and heated at 120 °C for 1 h. The chip was carefully removed from the solution and washed 3 times with ethanol and dried in air for 1 h. For the powder X-ray diffraction measurements (see Supplementary Note 1) the precipitate which results during the synthesis was separated via centrifugation, washed with DMF and ethanol, and dried under vacuum.

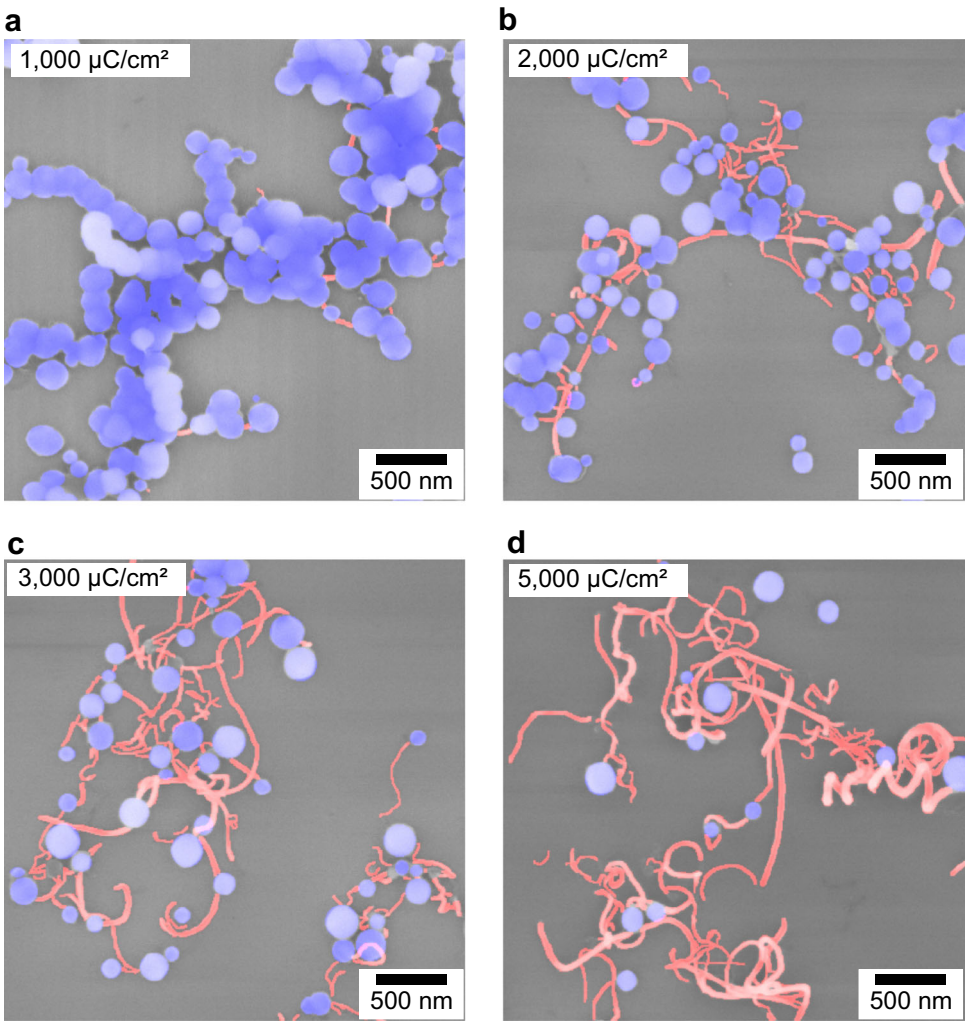

Fig. 3 | Impact of electron dose on MOF growth. After synthesis scanning electron microscope images of (prior to the synthesis) electron irradiated multi-walled carbon nanotubes (MWCNTs). The MOF area is colored in blue, and the bare MWCNT area is colored in red. The irradiation doses are **a** $D = 1000$ µC cm^{-2}, **b** $D = 2000$ µC cm^{-2}, **c** $D = 3000$ µC cm^{-2}, and **d** $D = 5000$ µC cm^{-2} all at $V_{acc} = 6$ kV. The higher the irradiation dose the stronger the MOF growth inhibition.

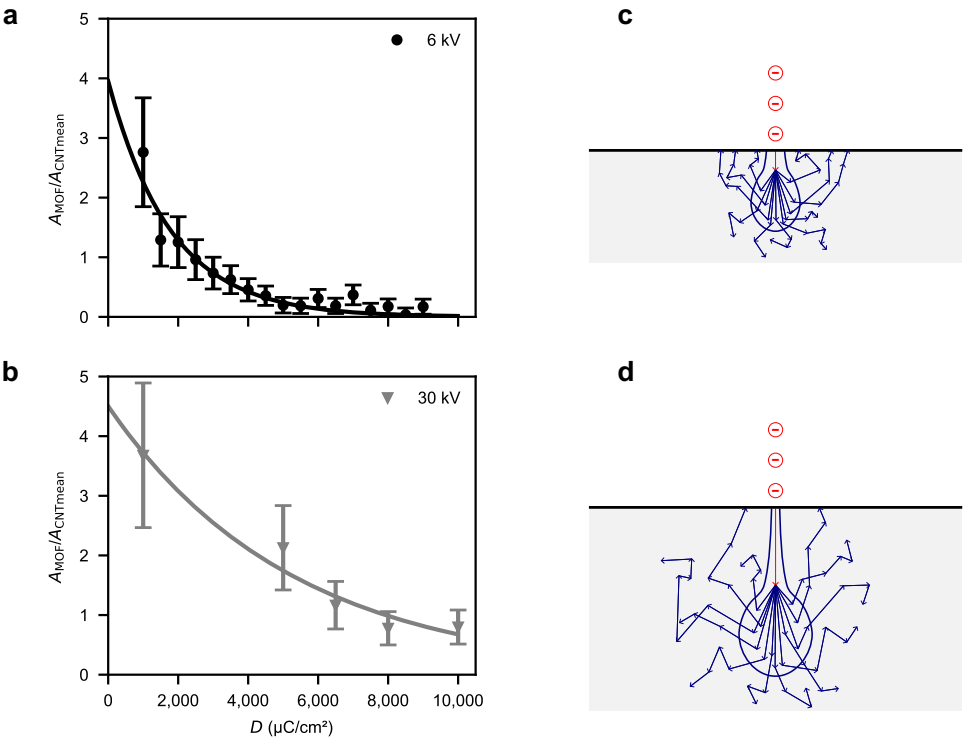

Fig. 4 | Influence of electron acceleration voltage. **a** Normalized MOF area A_{MOF} over the irradiation dose D at V_{acc} = 6 kV (dots) and **b** for V_{acc} = 30 kV (triangles). The higher the electron irradiation, the more suppressed the MOF growth. Solid lines are exponential fits of the form $A_{MOF}/A_{CNTmean} = A \cdot \exp(-D/g)$ with $A_{6kV} = 4$, $g_{6kV} = 1785$ μC cm^{-2}, $A_{30kV} = 4.5$, and $g_{30kV} = 5271$ μC cm^{-2}. The error bars denote the standard deviation calculated by the propagation of uncertainty using the individual standard deviations of A_{MOF} and $A_{CNTmean}$. **c** Schematic illustration of electron scattering within the substrate, with many electrons scattering near the surface (incident electrons colored in red and scattered electrons colored in blue). **d** Electron scattering for acceleration voltages higher (e.g., 30 kV) than in (**c**) (e.g., 6 kV). Electrons penetrate the substrate deeper and fewer electrons scatter near the surface, leading to less growth inhibition.

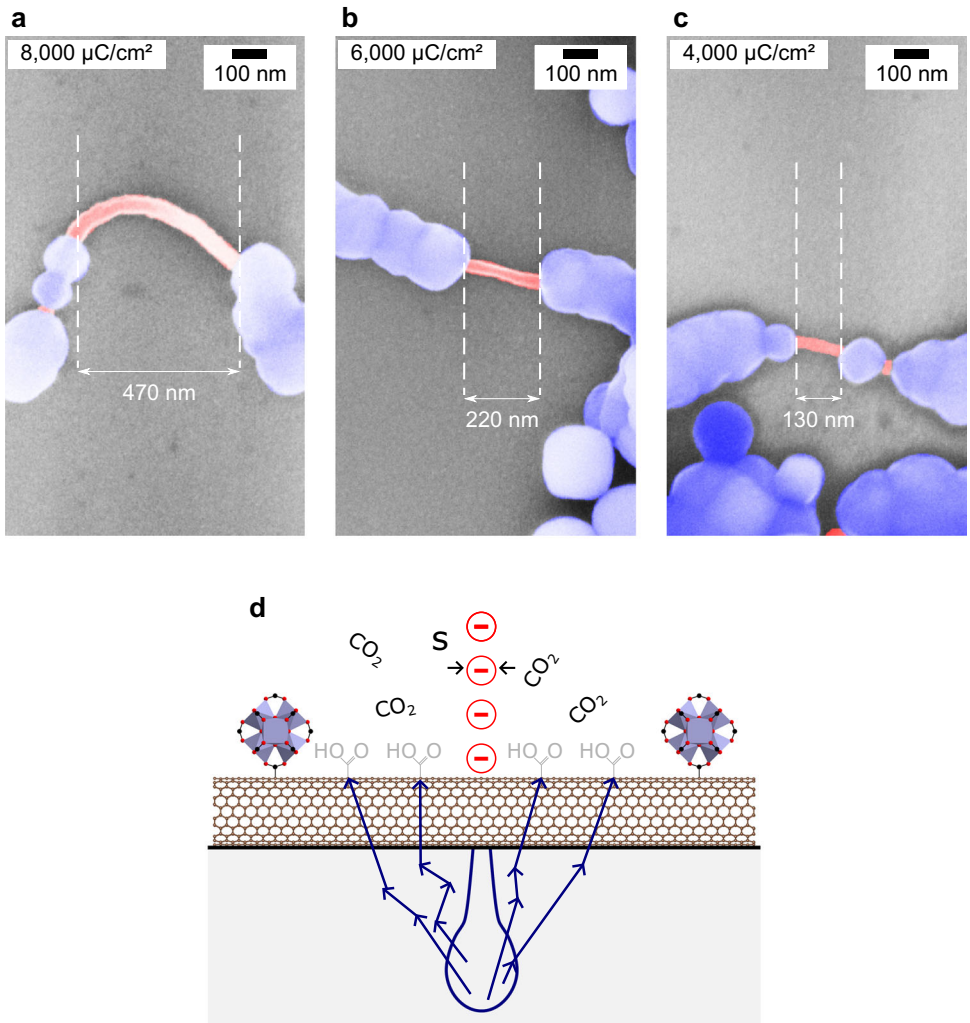

Fig. 5 | Locally controlled MOF growth. **a**, **b** and **c** show colored scanning electron microscopy images (MOF colored in blue, multi-walled carbon nanotube (MWCNT) colored in red) of locally irradiated, -COOH functionalized MWCNTs after UiO-66 synthesis. s = 200 nm wide stripes were irradiated by a V_{acc} = 6 kV electron beam, prior to the synthesis. The irradiation doses are **a** D = 8000 μC cm^{-2}, **b** D = 6000 μC cm^{-2}, and **c** D = 4000 μC cm^{-2}. MOF growth in the irradiated MWCNT areas is strongly inhibited. **d** Schematic side view of the stripe-irradiation process (not to scale) using stripe width s. Some backscattered electrons are off-axis scattered and reach the surface outside the irradiated width s. These electrons participate in the defunctionalization process, which could enlarge or reduce the MOF-free tube area.

Data availability

The data that support the findings of this work have been included in the manuscript and the Supplementary Information.

Received: 18 July 2023; Accepted: 5 March 2024;
Published online: 16 March 2024

References

1. Hendon, C. H., Rieth, A. J., Korzyński, M. D. & Dincă, M. Grand Challenges and future opportunities for metal-organic frameworks. *ACS Cent. Sci.* **3**, 554–563 (2017).
2. Wang, C., Liu, D. & Lin, W. Metal-organic frameworks as a tunable platform for designing functional molecular materials. *J. Am. Chem. Soc.* **135**, 13222–13234 (2013).
3. Furukawa, H., Cordova, K. E., O'Keeffe, M. & Yaghi, O. M. The chemistry and applications of metal-organic frameworks. *Science* **341**, 1230444 (2013).
4. Stavila, V., Talin, A. A. & Allendorf, M. D. MOF-based electronic and opto-electronic devices. *Chem. Soc. Rev.* **43**, 5994–6010 (2014).
5. Schulze, H. A., Hoppe, B., Schäfer, M., Warwas, D. P. & Behrens, P. Electrically conducting nanocomposites of carbon nanotubes and metal-organic frameworks with strong interactions between the two components. *ChemNanoMat* **5**, 1159–1169 (2019).
6. Mohmeyer, A. et al. Delamination and photochemical modification of a novel two-dimensional Zr-based metal-organic frameworks. *Chem. - A Eur. J.* **24**, 12848–12855 (2018).
7. Zhao, Z. et al. MXene assisted preparation of well-intergrown ZIF-67 membrane for helium separation. *J. Membr. Sci.* **652**, 120432 (2022).
8. Fan, H. et al. MOF-in-COF molecular sieving membrane for selective hydrogen separation. *Nat. Commun.* **12**, 38 (2021).
9. Naghdi, S. et al. Selective ligand removal to improve accessibility of active sites in hierarchical MOFs for heterogeneous photocatalysis. *Nat. Commun.* **13**, 282 (2022).
10. Achmann, S. et al. Metal-Organic frameworks for sensing applications in the gas phase. *Sensors* **9**, 1574–1589 (2009).
11. Bétard, A. & Fischer, R. A. Metal-organic framework thin films: from fundamentals to applications. *Chem. Rev.* **112**, 1055–1083 (2012).
12. Lei, J., Qian, R., Ling, P., Cui, L. & Ju, H. Design and sensing applications of metal-organic framework composites. *TrAC - Trends Anal. Chem.* **58**, 71–78 (2014).
13. Hoppe, B. et al. Graphene-like metal-organic frameworks: morphology control, optimization of thin film electrical conductivity and fast sensing applications. *CrystEngComm* **20**, 6458–6471 (2018).
14. Koo, W.-T., Jang, J.-S. & Kim, I.-D. Metal-organic frameworks for chemiresistive sensors. *Chem* **5**, 1938–1963 (2019).
15. Xie, L. S., Skorupskii, G. & Dinca, M. Electrically conductive metal-organic frameworks. *Chem. Rev.* **120**, 8536–8580 (2020).
16. Li, W.-H., Deng, W.-H., Wang, G.-E. & Xu, G. Conductive MOFs. *EnergyChem* **2**, 100029 (2020).
17. Jo, Y. et al. MOF-based chemiresistive gas sensors: toward new functionalities. *Adv. Mater.* **35**, 2206842 (2023).
18. Talin, A. A. et al. Tunable electrical conductivity in metal-organic framework thin-film devices. *Science* **343**, 66–69 (2014).
19. Gonçalves, J. M. et al. Recent trends and perspectives in electrochemical sensors based on MOF-derived materials. *J. Mater. Chem. C.* **9**, 8718–8745 (2021).
20. Liu, X.-W., Sun, T.-J., Hu, J.-L. & Wang, S.-D. Composites of metal-organic frameworks and carbon-based materials: preparations, functionalities and applications. *J. Mater. Chem. A* **4**, 3584–3616 (2016).
21. Iijima, S. Carbon nanotubes: past, present, and future. *Phys. B: Condens. Matter* **323**, 1–5 (2002).
22. Collins, P. G., Hersam, M., Arnold, M., Martel, R. & Avouris, P. Current saturation and electrical breakdown in multiwalled carbon nanotubes. *Phys. Rev. Lett.* **86**, 3128–3131 (2001).
23. Chronopoulos, D. D. et al. Carbon nanotube based metal-organic framework hybrids from fundamentals toward applications. *Small* **18**, 2104628 (2022).
24. Kim, B. & Sigmund, W. M. Functionalized multiwall carbon nanotube/gold nanoparticle composites. *Langmuir* **20**, 8239–8242 (2004).
25. Wang, M. Q., Zhang, Y., Bao, S. J., Yu, Y. N. & Ye, C. Ni(II)-based metal-organic framework anchored on carbon nanotubes for highly sensitive non-enzymatic hydrogen peroxide sensing. *Electrochim. Acta* **190**, 365–370 (2016).
26. Wang, S., Xue, Y., Yu, Z., Huang, F. & Jin, Y. Layered 2D MOF nanosheets grown on CNTs substrates for efficient nitrite sensing. *Mater. Today Chem.* **30**, 101490 (2023).
27. Chappanda, K. N. et al. The quest for highly sensitive QCM humidity sensors: the coating of CNT/MOF composite sensing films as case study. *Sens. Actuators B: Chem.* **257**, 609–619 (2018).
28. Winarta, J. et al. A decade of UiO-66 research: a historic review of dynamic structure, synthesis mechanisms, and characterization techniques of an archetypal metal-organic framework. *Cryst. Growth Des.* **20**, 1347–1362 (2020).
29. Sang, X. et al. Interfacial growth of metal-organic framework on carboxyl-functionalized carbon nanotubes for efficient dye adsorption and separation. *Anal. Methods* **12**, 4534–4540 (2020).
30. Chang, T. et al. Iridium-functionalized metal-organic framework nanocrystals interconnected by carbon nanotubes competent for electrocatalytic water oxidation. *ChemCatChem* **14**, e202200199 (2022).
31. Wang, Y., Wu, Y., Xie, J., Ge, H. & Hu, X. Multi-walled carbon nanotubes and metal-organic framework nanocomposites as novel hybrid electrode materials for the determination of nano-molar levels of lead in a lab-on-valve format. *Analyst* **138**, 5113–5120 (2013).
32. Tasis, D., Tagmatarchis, N., Bianco, A. & Prato, M. Chemistry of carbon nanotubes. *Chem. Rev.* **106**, 1105–1136 (2006).
33. Bitter, J. L., Yang, J., Beigzadeh Milani, S., Jafvert, C. T. & Fairbrother, D. H. Transformations of oxidized multiwalled carbon nanotubes exposed to UVC (254 nm) irradiation. *Environ. Sci.: Nano* **1**, 324–337 (2014).
34. Ruiz-Zambrana, C. L., Malankowska, M. & Coronas, J. Metal organic framework top-down and bottom-up patterning techniques. *Dalton Trans.* **49**, 15139–15148 (2020).
35. Keitz, B. K., Yu, C. J., Long, J. R. & Ameloot, R. Lithographic deposition of patterned metal-organic framework coatings using a photobase generator. *Angew. Chem. Int. Ed.* **53**, 5561–5565 (2014).
36. Stassen, I. et al. Chemical vapour deposition of zeolitic imidazolate framework thin films. *Nat. Mater.* **15**, 304–310 (2016).
37. Tu, M. et al. Direct X-ray and electron-beam lithography of halogenated zeolitic imidazolate frameworks. *Nat. Mater.* **20**, 93–99 (2021).
38. Miao, Y. & Tsapatsis, M. Electron beam patterning of metal-organic frameworks. *Chem. Mater.* **33**, 754–760 (2021).
39. Miao, Y. et al. Solvent-free bottom-up patterning of zeolitic imidazolate frameworks. *Nat. Commun.* **13**, 420 (2022).
40. Doherty, C. M. et al. Using functional nano- and microparticles for the preparation of metal-organic framework composites with novel properties. *Acc. Chem. Res.* **47**, 396–405 (2014).
41. Buso, D., Nairn, K. M., Gimona, M., Hill, A. J. & Falcaro, P. Fast synthesis of MOF-5 microcrystals using sol-gel SiO2 nanoparticles. *Chem. Mater.* **23**, 929–934 (2011).
42. Falcaro, P. et al. A new method to position and functionalize metal-organic framework crystals. *Nat. Commun.* **2**, 237 (2011).
43. Butz, B., Dolle, C., Halbig, C. E., Spiecker, E. & Eigler, S. Highly intact and pure oxo-functionalized graphene: synthesis and electron-beam-induced reduction. *Angew. Chem. Int. Ed.* **55**, 15771–15774 (2016).
44. Chang, T. H. P. Proximity effect in electron-beam lithography. *J. Vac. Sci. Technol.* **12**, 1271–1275 (1975).

Acknowledgements
This work was funded by the Deutsche Forschungsgemeinschaft (DFG, German Research Foundation) under Germany's Excellence Strategy-EXC 2123 Quantum Frontiers-390837967 and EXC 2122 PhoenixD-390833453. A.H. is grateful for being funded by the Hannover School for Nanotechnology (HSN) at the Laboratory of Nano and Quantum Engineering (LNQE). The HSN is funded by the Ministry of Science and Culture of Lower Saxony.

Author contributions
M.J.D. prepared the samples, performed data analysis, and wrote the manuscript. N.E.A. assisted in the sample preparation. A.H. performed the UiO-66 synthesis, PXRD characterization and assisted in XPS data interpretation. A.S. performed and interpreted the XPS measurements. P.B. supervised the UiO-66 synthesis. R.J.H. supervised the data analysis, data interpretation, and the writing of the manuscript.

Funding
Open Access funding enabled and organized by Projekt DEAL.

Competing interests
The authors declare no competing interests.

Additional information
Supplementary information The online version contains supplementary material available at https://doi.org/10.1038/s43246-024-00473-9.

Correspondence and requests for materials should be addressed to Marvin J. Dzinnik.

Peer review information *Communications Materials* thanks Alexander Star and the other, anonymous, reviewer(s) for their contribution to the peer review of this work. Primary Handling Editors: Natalia Shustova and Jet-Sing Lee. A peer review file is available.